Chinese Chemical Letters 37 (2026) 111878

Contents lists available at ScienceDirect

Chinese Chemical Letters

journal homepage: www.elsevier.com/locate/cclet

Engineering a garlic-derived nanovesicle/microneedle system to boost melanoma immunotherapy through self-amplifying cell death activation and immune remodelling

Jing Li[a], Jie Wang[a], Bingqian Li[a], Meng Long[a], Xiumei Liu[a], Dengxuan Mao[a], Patrick Pan[b], Ying Liu[a], Zimei Wu[b,*], Yaqi Lyu[a,*], Nianping Feng[a,*]

[a] School of Pharmacy, Shanghai University of Traditional Chinese Medicine, Shanghai 201203, China
[b] School of Pharmacy, Faculty of Medicine and Health Sciences, University of Auckland, Auckland 1023, New Zealand

ARTICLE INFO

Article history:
Received 25 June 2025
Revised 21 September 2025
Accepted 23 September 2025
Available online 24 September 2025

Keywords:
Garlic-derived nanovesicles
Dissolving microneedles
Pyroptosis
Immunotherapy
Melanoma

ABSTRACT

Current immunotherapy for melanoma remains limited by low immunogenicity, immune-related toxicity, and an immunosuppressive tumor microenvironment (TME), necessitating more effective strategies to enhance treatment outcomes. Enhancing immunogenic cell death (ICD) induction with immune remodelling offers a promising approach to boost antitumor immunity. Here, we develop a transdermal microneedle (MN) system co-delivering garlic-derived nanovesicles (Ve) and immunomodulatory garlic polysaccharides (GP) to synergistically activate a self-reinforcing cell death pathway and reprogram the immunosuppressive TME. The dissolving MN platform enables efficient intratumoral delivery of Ve-fused thermosensitive liposomes (TSVL@PTX/ICG), loaded with paclitaxel (PTX) and the photosensitizer indocyanine green (ICG). Upon near-infrared (NIR) irradiation, ICG-mediated photothermal heating triggers rapid drug release, inducing pyroptosis *via* gasdermin E (GSDME) cleavage while amplifying photodynamic therapy (PDT)-driven mitochondrial damage. This dual cell death mechanism elicits robust ICD, releasing tumor antigens and damage-associated molecular patterns (DAMPs) to enhance dendritic cell activation and cytotoxic T-cell infiltration. Concurrently, GP reprograms tumor-associated macrophages (TAMs) from immunosuppressive M2 to pro-inflammatory M1 phenotypes, reshaping the TME into an immunostimulatory niche. This multi-modal approach, combining pyroptosis-driven ICD, PDT, and immune remodelling achieves potent antitumor immunity and melanoma suppression, highlighting the potential of plant-derived therapeutics in cancer immunotherapy.

© 2026 Published by Elsevier B.V. on behalf of Chinese Chemical Society and Institute of Materia Medica, Chinese Academy of Medical Sciences.

Immunotherapy, such as immune checkpoint inhibitors (ICIs), adoptive cellular immunotherapy (ACT), cancer vaccines has revolutionized the treatment of melanoma [1,2]. However, low immunogenicity, immune toxicity and immunosuppressive tumor microenvironment (TME) limit its clinical application [3]. Generally, many anticancer immunotherapies exploit immunogenic cell death (ICD) to activate antitumor immune responses by triggering the release of tumor-associated antigens (TAAs) and damage-associated molecular patterns (DAMPs) from dying tumor cells [4]. These signals promote antigen-presenting cell (APC) activation and subsequent cytotoxic T lymphocyte (CTL)-mediated tumor elimination. Thus, inducing a robust ICD is the key to improving tumor immunogenicity.

Pyroptosis is a lytic, pro-inflammatory form of programmed cell death initiated when inflammatory caspases cleave gasdermin (GSDM) proteins, generating N-terminal fragments that oligomerize to form membrane pores. These pores disrupt cellular integrity, leading to the release of antigen and potent cytokines (*e.g.*, interleukin-1 beta (IL-1β), IL-18), thereby eliciting a robust antitumor immune response [5]. However, only certain cytotoxic drugs or photosensitizers are pyroptosis inducers and they often fail to achieve robust immunostimulation [6]. On one hand, their efficacy is limited by drug resistance, leading to insufficient DAMPs release incomplete pyroptosis induction. On the other hand, uncontrollable pyroptosis activation can induce pathological inflammation and paradoxically promote an immunosuppressive TME [7,8]. Therefore, sufficient pyroptosis induction, by ensuing robust DAMP release through combination therapies and adjuvant immunomodulator, while maintaining precise control is critical for effective cancer immunotherapy.

* Corresponding authors.
E-mail addresses: z.wu@auckland.ac.nz (Z. Wu), ylyu07@shutcm.edu.cn (Y. Lyu), npfeng@shutcm.edu.cn (N. Feng).

https://doi.org/10.1016/j.cclet.2025.111878
1001-8417/© 2026 Published by Elsevier B.V. on behalf of Chinese Chemical Society and Institute of Materia Medica, Chinese Academy of Medical Sciences.

Herbal plants have been used for centuries in traditional medicine systems for their therapeutic properties, including immune regulation and disease prevention. Garlic (*Allium sativum* L.) is a globally recognized functional food and has been utilized for millennia to treat ailments such as colds, influenza, dysentery, and cancer [9]. Garlic-derived compounds have been found to exhibit dual regulatory effects on pyroptosis, garlic oil and diallyl trisulfide (DATS) suppress pyroptosis in inflammatory diseases like lung injury and alcoholic liver disease by boosting H_2S, while DATS induce pyroptosis in lung cancer cells *via* reactive oxygen species (ROS) production and NOD-like receptor family pyrin domain containing 3 (NLRP3) inflammasome activation [10–12]. Beyond this, modern research also reveals that garlic extracts exhibit significant immunomodulatory activities. Garlic polysaccharides (GP) have been reported to exert immunomodulatory effects through various mechanisms, including the ability to repolarize tumor-associated macrophages (TAMs) [13], which is crucial in regulating immune and inflammatory responses [14]. With emerging biotechnology, plant-derived extracellular vesicles (EVs) have shown great potential in disease treatment owing to their unique natural biological characteristics. Previous study found that compared to fresh garlic extract, garlic-derived nanoparticles was more capable of activating $\gamma\delta$ T cells, promoting IFN-γ secretion after oral administration [15].

Despite these promising properties, the clinical translation of garlic-based therapies for melanoma remains hindered by inefficient targeted delivery of its bioactive components. Conventional oral administration fails to achieve sufficient tumor-site accumulation, highlighting the need for advanced delivery strategies to maximize the therapeutic potential of garlic-derived compounds in melanoma treatment. Microneedles (MNs) represent an innovative transdermal delivery platform that creates transient micropores in the stratum corneum while avoiding stimulation of pain receptors and blood vessels, thereby combining the efficacy of hypodermic injection with the patient compliance of transdermal patches [16]. Recent advancements have highlighted the remarkable potential of MN-based systems for precise and efficient drug delivery [17,18]. In this study, we developed a micro-nano immunomodulatory system utilizing dissolving MNs for transdermal co-delivery of garlic-derived components and cytotoxic agents to treat melanoma (Scheme S1 in Supporting information). GP and garlic-derived extracellular vesicles (Ve) were extracted from garlic. Ve was fused with thermosensitive liposomes (TSL@PTX/ICG) containing chemotherapeutic agent paclitaxel (PTX) and a photosensitizer indocyanine green (ICG), to form TSVL@PTX/ICG nanoparticles, which were loaded in GP fabricated MNs. The thermo-sensitive liposomes (TSL) can release contents at specific temperatures. By incorporating ICG, a photothermal conversion agent in TSL, fast release of encapsulated components and PDT-induced tumor death can be achieved upon exposure to near-infrared (NIR) irradiation [19,20]. Thus, the strategy involving membrane fusion of TSL@PTX/ICG with Ve enables the content in Ve and PTX to be rapidly released in the tumor site upon laser-induced heating, resulting in locally high concentrations to activate pyroptosis, inducing strong ICD by releasing DAMPs and inflammatory cytokines to recruit immune cells in TME. Notably, pyroptotic GSDM protein amplified mitochondrial damage induced by PDT [21], by forming pores on the mitochondrial membrane, creating a positive feedback loop that potentiated ICD. Furthermore, GP reverses the immunosuppressive TME by repolarization of M2-type TAM to pro-inflammatory M1-type, which stimulates the secretion of pro-inflammatory cytokines in TME, thereby converting the immunosuppressive TME into an immunostimulatory niche that enhances T lymphocyte infiltration and tumor clearance. This report represents the first study of a micro-nano immunomodulator fabricated from garlic-derived components and provides a multi-modal approach that achieves comprehensive tumor control through coordinated cytotoxic, immunogenic, and immunomodulatory actions.

TSVL@PTX/ICG was prepared by physical co-extrusion of Ve and TSL@PTX/ICG. The phase transition temperature (T_m) of TSL was optimized to 41.8 °C using an 8:2 HSPC:PC-98T ratio to ensure thermosensitivity while minimizing thermal damage (Table S1 in Supporting information). Ve was isolated *via* differential ultracentrifugation. Lyophilized Ve presented as light-yellow solid, and its solution showed the Tyndall effect (Fig. S1 in Supporting information). Bicinchoninic acid (BCA) assay confirmed a protein content of 0.30 ± 0.03 mg per 1 mg of lyophilized Ve. As increasing Ve protein concentration reduced the size of TSVL@PTX/ICG, thus 1 mg/mL was selected as the optimal concentration to prepare TSVL@PTX/ICG (Fig. S2 in Supporting information).

Under transmission electron microscopy (TEM), TSL@PTX/ICG displayed uniform spherical structures, while Ve exhibited "teacup-like" morphology typical of plant-derived extracellular vesicles [22]. The fused TSVL@PTX/ICG demonstrated enhanced membrane definition compared to conventional liposomes (Fig. 1A). Size distribution analysis by dynamic light scattering (DLS) and nanoparticle tracking analysis (NTA) showed excellent consistency, with diameters of TSL@PTX/ICG, Ve, and TSVL@PTX/ICG of 82.0 ± 0.51, 138.3 ± 4.53, and 118.4 ± 6.34 nm, all exhibiting narrow polydispersity (PDI < 0.3) (Figs. 1B and C). To confirm successful fusion, we employed dual-fluorescence labelling with coumarin-6 (C6, green) for TSL and DiI (red) for Ve. Confocal laser scanning microscopy (CLSM) demonstrated complete colocalization of fluorescence signals in TSVL@PTX/ICG, verifying membrane integration (Fig. 1D) [23]. Zeta potential measurements revealed a moderate increase in surface negative charge, with -7.93 ± 0.104 mV for TSVL@PTX/ICG compared to TSL@PTX/ICG and Ve (Fig. 1E). Fourier transform infrared (FTIR) spectrum analysis identified new vibrational bands at 1546.43 and 1529.18 cm^{-1} in TSVL@PTX/ICG, absent in either component, confirming molecular-level interactions during fusion. The preservation of characteristic peaks indicated structural integrity of the constituent materials (Fig. 1F) [24]. Notably, T_m increased from 41.8 °C to 44.6 °C post-fusion (Fig. 1G). This increase may be attributed to the modified membrane packing density of TSVL@PTX/ICG due to fusion process. Photothermal evaluation under 808 nm NIR irradiation demonstrated precise temperature control, with TSVL@PTX/ICG reaching and maintaining 44 °C for 10 min, which is ideal for mild photothermal therapy while avoiding tissue damage (Fig. 1H and Fig. S3 in Supporting information). This temperature profile, combined with excellent photostability, highlights the system's potential for precise thermal-triggered drug release in cutaneous oncology application.

The drug loading capacity of TSVL@PTX/ICG was determined to be 5.93 % for PTX and 3.60 % for ICG. Under 808 nm irradiation, TSVL@PTX/ICG exhibited temperature-responsive drug release, achieving (95.03 ± 3.08) % PTX release within 24 h, with an initial burst release occurring within the first 2 h. In contrast, only (76.48 ± 2.28) % PTX was released without NIR irradiation (Fig. 1I). A comparable release profile was observed for TSL@PTX/ICG (Fig. 1J), confirming that the presence of ICG significantly enhanced both the rate and extent of PTX release through photothermal conversion. These results demonstrate that TSVL@PTX/ICG maintains excellent thermosensitivity after vesicle fusion while gaining enhanced drug release capabilities.

Following Ve isolation by ultracentrifugation, the supernatant was processed for GP extraction. The characterization of GP can be found in Supporting information. While GP demonstrated considerable mechanical strength, its inherent brittleness posed challenges for MN fabrication. To address this, we developed a composite system by blending GP with hyaluronic acid (HA), which significantly improved the material's elasticity and structural integrity [25,26]. Through systematic optimization based on MN

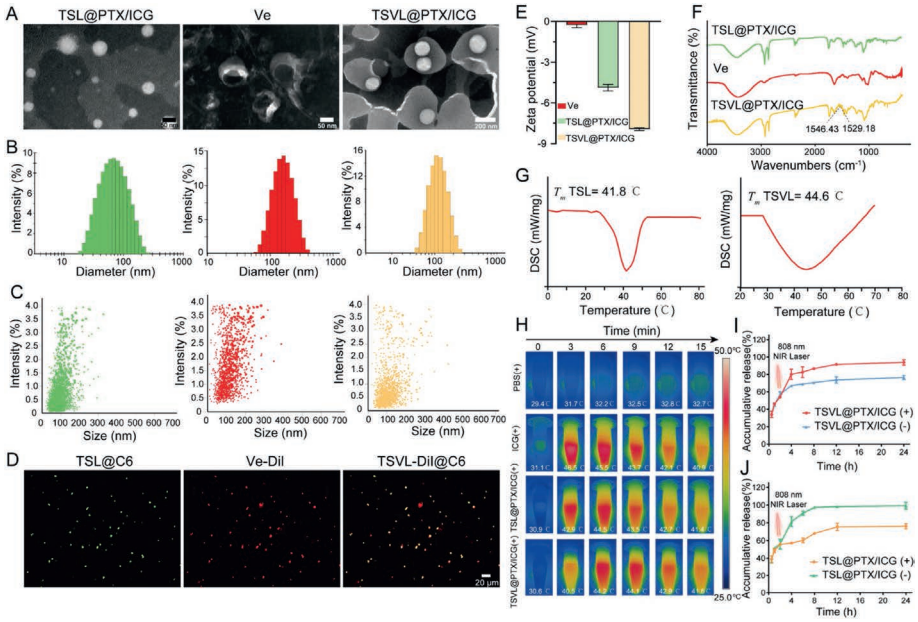


Fig. 1. Characterization. (A) Representative TEM image, (B) hydration diameter and (C) size distribution of TSL@PTX/ICG, Ve, and TSVL@PTX/ICG. Scale bar: 50, 50, 200 nm, respectively. (D) Fluorescence images of TSL@C6, Ve-DiI, and TSVL-DiI@C6. Scale bar: 20 μm. (E) Zeta potentials. (F) FTIR spectra. (G) DSC analysis. (H) Thermographic images under NIR irradiation of 808 nm (2.75 W/cm^2, 15 min). PTX release from (I) TSVL@PTX/ICG and (J) TSL@PTX/ICG upon NIR irradiation of 808 nm (2.75 W/cm^2, 15 min). (−) indicates no NIR irradiation; (+) indicates NIR irradiation applied. All the quantitative data are means ± SD ($n = 3$).

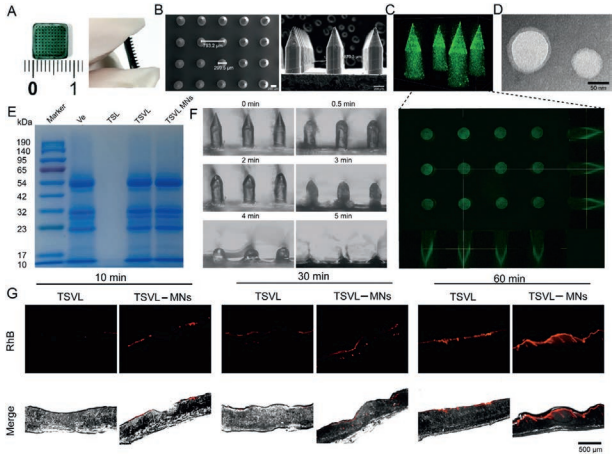


Fig. 2. Characterization of MN patch. (A) Appearance and (B) representative SEM image of TSVL@PTX/ICG MNs. Scale bar: 200 μm. (C) 3D reconstructed images of TSVL@C6 loaded MNs. (D) Representative TEM image of TSVL@PTX/ICG dissolved in MN tips. Scale bar: 50 nm. (E) SDS-PAGE protein analysis. (F) Dissolution processes of the MNs (magnification, ×40). (G) Distribution of RhB fluorescence in mice skin following treatment of TSVL@RhB or TSVL@RhB loaded MNs. Scale bar: 500 μm.

performance criteria (Table S2 in Supporting information), a GP-to-HA ratio of 3:2 (w/w) at a total concentration of 30 % was used to build MN tips for loading TSVL@PTX/ICG. The final MN base was formulated with 20 % HA (Table S3 in Supporting information).

The MN patch featured a 10 × 10 array of uniformly spaced needles (Fig. 2A). Representative scanning electron microscope (SEM) images revealed well-defined, pencil-shaped needle tips with consistent morphology and no structural deformations. The diameter of each tip was 299.5 μm, and the height was 870.3 μm. The distance between the tips was 793.2 μm (Fig. 2B). Fluorescence imaging of TSVL@C6 MNs demonstrated homogeneous drug distribution throughout the array, as uniform green fluorescence was observed in 3D reconstructions (Fig. 2C). TEM and sodium dodecyl sulfate-polyacrylamide gel electrophoresis (SDS-PAGE) analysis confirmed TSVL@PTX/ICG maintained its spherical nanostructure and protein contents within the MNs, indicating preservation of Ve integrity during fabrication (Figs. 2D and E). The MN system exhibited optimal dissolution kinetics, completely dissolving within 5 min (Fig. 2F), showing the potential to rapidly release payloads in the dermal layers. To evaluate the penetration capability, MNs loaded with rhodamine B-labelled TSVL (TSVL@RhB MNs) were inserted into mice skin, and the penetration depth was monitored by tracking the red fluorescence. Compared to TSVL@RhB smeared on the skin, the fluorescence of TSVL@RhB MNs distributed much deeper into the skin and released rapidly (Fig. 2G), suggesting MNs directly delivered TSVL@RhB under the stratum corneum [27]. Moreover, the pinholes from TSVL@RhB MNs were uniform in size (Fig. S7C in Supporting information), and the pinhole shape was consistent with the shape of tips, showing TSVL@RhB MNs maintained their integrity during piercing process. The maximum penetration depth was 400 μm (Fig. S7D in Supporting information).

In the *in vitro* therapeutic efficacy assessment, Ve exhibited no cytotoxicity below the concentration of 125 μg/mL (Fig. S9A in Supporting information). TSVL@PTX/ICG demonstrated dose-dependent cytotoxicity. The half-maximal inhibitory concentration (IC_{50}) of PTX contained in TSVL@PTX/ICG was 1.70 μg/mL, significantly lower than the free PTX (3.07 μg/mL) and PTX in TSL@PTX/ICG (4.37 μg/mL) (Fig. 3A and Fig. S9B in Supporting information). Given NIR-induced PTT's ability to penetrate deep tissues [28], we assessed TSVL@PTX/ICG's depth-dependent efficacy using 3D B16 melanoma spheroids. Live/dead staining showed stronger red fluorescence (cell death) in the spheroid core for TSVL@PTX/ICG (+), alongside reduced live-cell signal (Fig. 3B). Annexin V/PI staining revealed Ve induced apoptosis comparably to free PTX (Figs. 3C and D), TSVL@PTX/ICG (−) showed 1.69- and 1.97-fold higher apoptosis than TSL@PTX/ICG and free PTX, demonstrating Ve's pro-apoptotic effect and synergy with PTX. NIR irradiation further enhanced apoptosis rate to 39.7 %, confirming photothermal-chemotherapeutic synergy.

Emerging evidence suggests that some chemotherapeutic agents can trigger caspase-3-dependent pyroptosis when gasdermin E (GSDME) is expressed [29,30]. In B16 melanoma, a relatively

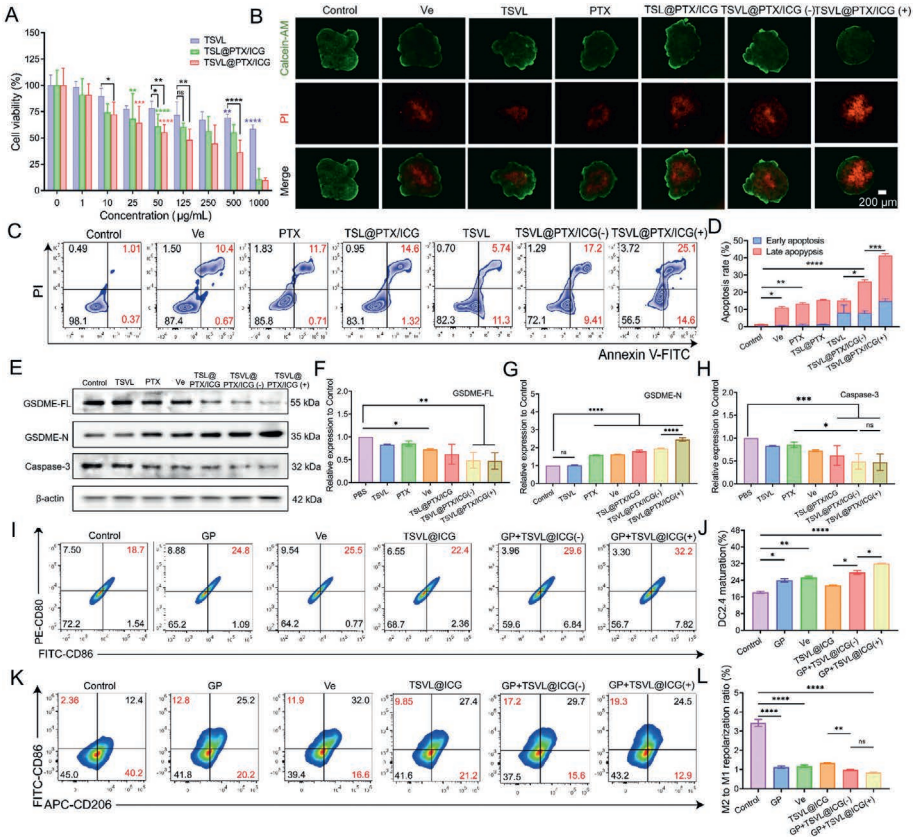


Fig. 3. *In vitro* evaluation of anti-tumor effects. (A) Cytotoxicity to B16 after 48-h incubation of TSVL, TSL@PTX/ICG and TSVL@PTX/ICG ($n = 5$). (B) Live/dead staining of B16 tumor spheroids treated with different formulations. Scale bar: 200 μm. (C) Apoptosis of B16 cells determined by Annexin V-FITC/PI staining. (D) Quantitative apoptosis rate in Fig. 3C. (E) WB analysis of caspase-3, GSDME-FL and GSDME-N. β-Actin was used as a loading control. (F–H) Quantitative analysis of the expression of (F) GSDME-FL, (G) GSDME-N, and (H) caspase-3 by ImageJ. (I) Expression of $CD80^+$ and $CD86^+$ on DC2.4 cells determined by flow cytometry. (J) Quantitative analysis of DC maturation rate in Fig. 3I. (K) Expression of $CD86^+$ and $CD206^+$ on RAW264.7 macrophage cells determined by flow cytometry. (L) Quantitative analysis of macrophage repolarization rate in Fig. 3K. All the quantitative data are means ± SD. $^*P < 0.05$, $^{**}P < 0.01$, $^{***}P < 0.001$, $^{****}P < 0.0001$, ns, not significant.

high baseline expression of GSDME was observed in untreated cells (Figs. 3E and F), providing a foundation for its cleavage when caspase-3 is activated. After treatment, a decreased expression level of caspase-3 was observed. Both Ve and PTX independently promoted pyroptosis, evidenced by the decrease of GSDME-FL (full length) and the increase of GSDME-N. Their combination in TSVL@PTX/ICG (−) showed additive effects (Figs. 3E–H). The significant amplification of pyroptotic markers in the TSVL@PTX/ICG (+) group demonstrates that NIR irradiation potentiates caspase-3-mediated pyroptosis. To investigate the mechanism, ROS levels showed NIR irradiation triggered significant ROS in ICG (+) and TSVL@PTX/ICG (+) groups (Fig. S10 in Supporting information). Ve alone also induced ROS, revealing garlic components' oxidative properties. Recent studies reported GSDME-N fragments exhibit dual targeting capacity, perforating both plasma and mitochondrial membranes [31]. In JC-1 staining, untreated cells showed intact mitochondria (red aggregates), while treatments with different formulations caused green monomers (Fig. S11 in Supporting information), with TSVL@PTX/ICG (+) demonstrating the most pronounced mitochondrial depolarization, confirming severe mitochondrial dysfunction. Collectively, NIR irradiation of TSVL@PTX/ICG induced pyroptosis enhanced mitochondrial damage, creating a synergistic self-amplification cycle that orchestrates programmed cell death by caspase-3 activation, maximizing ICD efficiency.

Previous reports revealed plant polysaccharides exhibit dual immunomodulatory effects through dendritic cells (DC) maturation and macrophage repolarization [32–34]. As depicted in Figs. 3I and J, GP and Ve significantly upregulated DC2.4 maturation markers, showing fold increases of 1.3 to CD80 and 1.4 to CD86, respectively. NIR-irradiated TSVL@ICG combinations resulted in even higher CD80 and CD86 expressions, showing the maximal enhancement of DC2.4 maturation. Macrophages are highly adaptable immune cells capable of adopting distinct functional phenotypes in response to environmental cues. In chronic or excessive inflammation, macrophages tend to polarize toward the M2 phenotype, which suppresses antitumor immunity and contributes to immunosuppressive TME. In contrast, repolarizing M2-type macrophages to the M1 phenotype can shift this immunosuppressive TME toward a more active, immune-stimulatory state [35]. In our study, treatments induced a pronounced M2-to-M1 macrophage shift, as evidenced by increased $CD86^+$ and decreased $CD206^+$ populations [36]. Notably, the GP+TSVL@ICG (+) combination reduced M2/M1 ratio from 3.4 to 0.8 (Figs. 3K and L), suggesting potential immunomodulation on macrophage polarization. Collectively, these findings indicate that GP+TSVL@ICG (+) promotes an immunostimulatory phenotype through dual effects on DC activation and macrophage repolarization. This immunomodulatory platform represents a promising strategy for melanoma immunotherapy with tumor-specific immunity potential.

The *in vivo* antitumor efficacy of TSVL@PTX/ICG MNs was systematically evaluated in B16 melanoma-bearing mice. All animal procedures followed the guidelines set by the Regional Ethics Committee for Animal Experiments and adhered to the Care Regulations approved by the Institutional Animal Care and Use Committee at Shanghai University of Traditional Chinese Medicine (No.

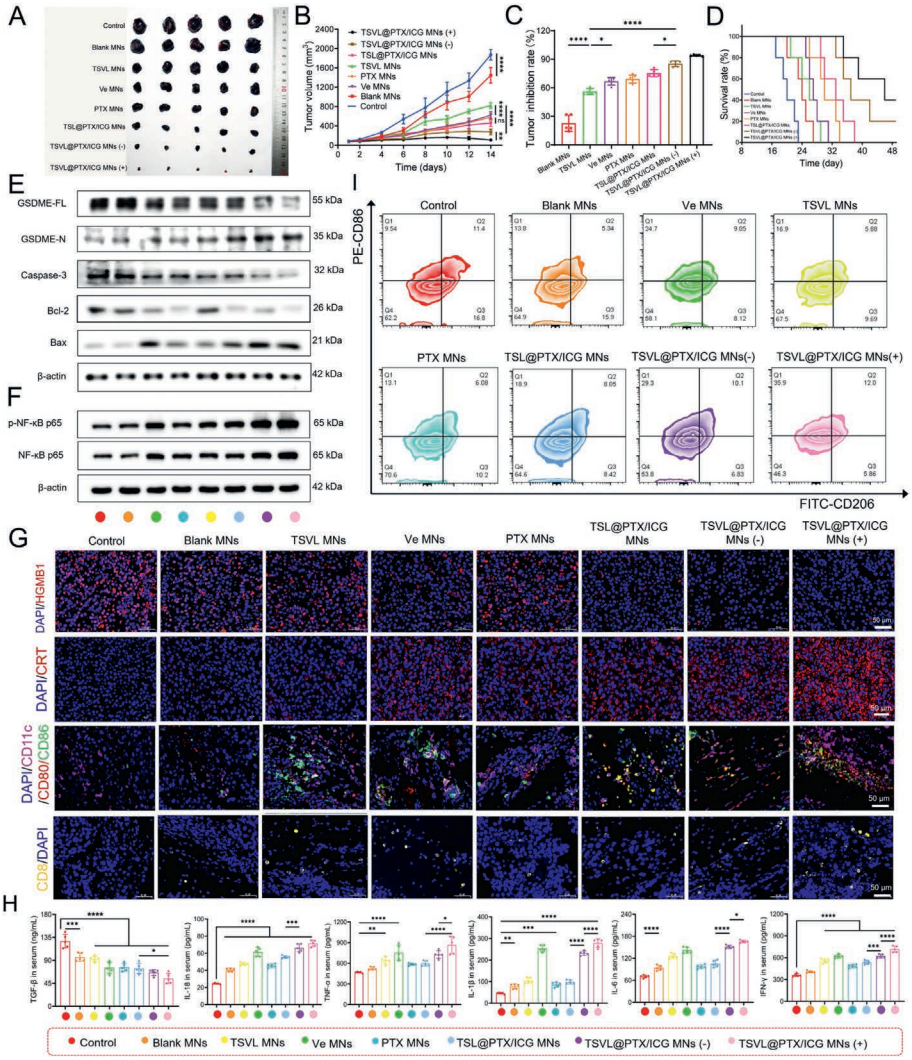


Fig. 4. *In vivo* anti-tumor efficacy of TSVL@PTX/ICG MNs. (A) Photographs of collected tumors. (B) Tumor growth curves of B16 tumor-bearing mice ($n = 5$). (C) Tumor inhibition rate. (D) Survival curves of B16 tumor-bearing mice. WB analysis of (E) GSDME-FL, GSDME-N, caspase-3, Bcl-2, BAX and (F) NF-κB p65, p-NF-κB p65. β-Actin was used as a loading control. (G) Immunofluorescence staining of tumor tissues collected on day 14 after treatments (scale bar: 50 μm). (H) Levels of TGF-β, IL-18, TNF-α, IL-1β, IL-6, and IFN-γ in mice serum collected from B16 tumor-bearing mice on day 14 after treatments, determined by ELISA ($n = 5$). (I) Representative FCM plots of F4/80$^+$CD206$^+$CD86$^+$ macrophages in B16 tumors after different treatments. All the quantitative data are means ± SD. $^*P < 0.05$, $^{**}P < 0.01$, $^{***}P < 0.001$, $^{****}P < 0.0001$.

PZSHUTCM2403200003). Following the treatment protocol (Fig. S13 in Supporting information), mice were treated with different formulations and NIR irradiation (808 nm, 1.25 W/cm^2, 10 min) was applied 1 h post-MN insertion to allow wound healing, with real-time temperature monitoring to ensure temperature was maintained below the 45 °C safety threshold (Fig. S14 in Supporting information). Blank MNs showed minimal effect, while Ve-MNs and TSL@PTX/ICG MNs achieved the inhibition rate of 66.83 % and 75.42 %, respectively (Figs. 4A–C). TSVL@PTX/ICG MNs (+) exhibited superior tumor suppression (94.17 % inhibition) and extended median survival to 45 days *versus* 3 weeks for controls (Fig. 4D). All treatments maintained stable body weights, confirming preliminary safety (Fig. S15 in Supporting information). The anti-tumor activity was further studied in isolated tumors after the treatment was completed. H&E staining revealed extensive necrosis in the TSVL@PTX/ICG MNs (+) group (Fig. S16 in Supporting information). TUNEL assays confirmed massive apoptosis induction in PTX MNs, TSL@PTX/ICG MNs, TSVL@PTX/ICG MNs (−) and TSVL@PTX/ICG MNs (+) treated groups, indicating PTX was the main factor inducing apoptosis. The strongest green fluorescence signal in TSVL@PTX/ICG MNs (+) suggested the incorporation of PTX maximized the tumor apoptosis, showing the synergy between each component. Ki-67 is a biomarker indicating cell proliferation. Immunohistochemistry confirmed TSVL@PTX/ICG MNs (+) inhibited Ki-67 more effectively than any single treatment or treatment without NIR irradiation (Fig. S16 in Supporting information).

Western blot (WB) analysis revealed both PTX MNs and TSL@PTX/ICG MNs activated the intrinsic apoptotic pathway, as demonstrated by decreased Bcl-2 and caspase-3 expression alongside increased Bax levels (Fig. 4E and Fig. S17 in Supporting information). These treatments also induced pyroptosis, evidenced by elevated GSDME-N fragments. In TSVL@PTX/ICG MNs (−) treatment, a significantly higher level of GSDME-N was observed. In addition, the expression of Bcl-2 and caspase-3 decreased, while Bax was markedly increased, suggesting the strong activation of pyroptosis enhanced apoptosis by stimulating the intrinsic apoptotic pathway. Bcl-2 is primarily known for its anti-apoptotic function which maintains mitochondrial integrity by blocking the activity of pro-apoptotic proteins, such as Bax and cytostome C [37]. However, when GSDME-N is generated, it forms pores in the mitochondrial membrane, leading to the release of pro-apoptotic proteins and disrupting the Bcl-2/Bax balance, thereby activating the

Bcl-2-mediated apoptotic pathway. This crosstalk establishes a self-reinforcing death cycle where pyroptosis potentiates apoptosis and *vice versa*. Importantly, TSVL@PTX/ICG MNs (+) further enhanced this loop, demonstrating photothermal and photodynamic effects dramatically augment the ICD response.

The exposure of calreticulin (CRT) on tumor cell surfaces and the extracellular release of high mobility group box 1 (HMGB1) act as key DAMPs during ICD. HMGB1 is a non-histone nuclear protein that normally binds chromatin to maintain DNA architecture. During ICD, it is actively released from the nucleus [38]. Immunofluorescence analyses (Fig. 4G and Fig. S18A in Supporting information) revealed HMGB1-associated red fluorescence in tumor cells declined after each treatment, with the TSVL@PTX/ICG (+) group showing a 7.02-fold reduction relative to the control, confirming robust ICD induction. CRT functions as "eat-me" signals that facilitates DC recruitment and subsequent phagocytosis of dying cells [39]. Immunofluorescence analysis revealed differential CRT expression patterns across treatment groups (Fig. 4G and Fig. S18B in Supporting information). Blank MNs treatment elicited only weak CRT fluorescence, indicating minimal ICD induction primarily attributable to GP components. In contrast, the TSVL@PTX/ICG MNs (-) group showed superior CRT expression compared to TSL@PTX/ICG MNs, highlighting the synergistic ICD induction by combined Ve and PTX delivery. Maximum CRT exposure was achieved in the TSVL@PTX/ICG MNs (+) group, where NIR irradiation further amplified ICD markers, demonstrating the critical role of photodynamic activation in potentiating ICD [40,41].

Nuclear factor kappa-B (NF-κB) p65, a phosphorylation-regulated transcription factor subunit, is sequestered in the cytoplasm by inhibitor of κ-Bα (IκBα). Upon inflammatory or oxidative stimuli, IκB kinase (IKK)-mediated IκBα degradation releases p65, which undergoes phosphorylation-dependent nuclear translocation and binds κB sites to activate pro-inflammatory signalling [42,43]. After treatment, a marked upregulation of the ratio of phospho-NF-κB p65 (p-NF-κB p65) to total NF-κB p65 was observed (Fig. 4F and Fig. S19 in Supporting information), indicating robust activation of pro-inflammatory pathways within TME [44]. This inflammatory response triggers immune cv ell activation and subsequent cytokine release, including IL-18, tumor necrosis factor-α (TNF-α), IL-1β, and IL-6 [45]. These cytokines, in turn, amplify the inflammatory cascade by promoting the recruitment of immune cells to the site of inflammation, thereby influencing immunotherapeutic response. Cytokine profiling by enzyme-linked immunosorbent assay (ELISA) revealed Ve-containing formulations elicited stronger inflammatory responses compared to PTX-based treatments, as evidenced by significantly higher levels of IL-18, TNF-α, IL-1β, and IL-6 (Fig. 4H). Following TSVL@PTX/ICG (+) treatment, levels of IL-18, TNF-α, IL-1β, IL-6, and interferon-γ (IFN-γ) were significantly elevated in mouse serum, while transforming growth factor-β (TGF-β) level sharply decreased. The increased cytokine levels foster an immune-active environment that is conducive to DC maturation, macrophage repolarization, and T lymphocyte infiltration.

Building upon the demonstrated efficacy in inducing ICD and inflammatory responses, we further evaluated the immunomodulatory effects of TSVL@PTX/ICG (+). Immunofluorescence analysis of key immune markers revealed TSVL@PTX/ICG MNs (+) significantly enhanced co-expression of CD80/CD86 with CD11c$^+$ DCs, indicating robust DC maturation into functional APCs (Fig. 4G). Moreover, flow-cytometric quantification revealed the M1/M2 macrophage ratio rose from 0.46 to 4.70 after TSVL@PTX/ICG MN (+) treatment (Fig. 4I and Fig. S20 in Supporting information). Therefore, the dual modulation of DC maturation and macrophage repolarization establishes TSVL@PTX/ICG MNs (+) as a potent strategy for overcoming tumor-associated immunosuppression.

Unlike many cancers characterized by "cold" tumors with low immunogenicity, melanoma is classified as a "hot" tumor, often exhibiting a high density of tumor-infiltrating lymphocytes (TILs) within its TME. This property increases the detectability of the tumor by the immune system, potentially enhancing the immune response. Nevertheless, despite the presence of TILs in melanoma, the high clinical mortality rate suggests that these lymphocytes are either numerically inadequate or functionally deficient, impeding full tumor elimination [46,47]. Therefore, a key challenge in achieving comprehensive tumor eradication is to enhance both the quantity and functionality of TILs. CD8$^+$ T cells are key lymphocytes to attack tumor cells [48]. Our results demonstrated that TSVL@PTX/ICG MNs significantly enhanced CD8$^+$ CTL infiltration, with the NIR (−) group showing 177-fold greater CD8$^+$ T cell density compared to controls. The NIR (+) treatment group exhibited even more robust CTL activation with 213-fold increase, as quantified by fluorescence intensity analysis (Fig. 4G and Fig. S18C in Supporting information). Therefore, the above results indicate that TSVL@PTX/ICG MNs (+) can facilitate the maturation of DCs, promote the repolarizing of M2-type macrophages to M1-type macrophages, reprogram the immunosuppressive TME, and activate T cells, thereby eliciting full immune effector function.

In summary, we developed a novel micro-nano immunomodulatory system based on Ve and GP delivered *via* dissolving MNs for enhanced melanoma immunotherapy. This strategy synergistically combines pyroptosis-mediated ICD with tumor TME remodelling to overcome the limitations of conventional immunotherapy. The system's unique immunomodulatory capacity stems from its ability to establish a self-reinforcing pyroptosis/apoptosis loop through mitochondrial targeting, where pyroptotic pore formation amplifies the signalling. This dual death mechanism not only enhances APCs maturation but also effectively reprograms the immunosuppressive TME through the secretion of inflammatory cytokines, leading to significantly improved cytotoxic T lymphocyte infiltration and function. By harnessing the natural immunostimulatory properties of garlic components within an advanced drug delivery platform, we achieved superior therapeutic efficacy while maintaining an excellent safety profile. This study represents a significant advancement in herbal medicine adjuvanted cancer immunotherapy, offering a promising green approach for the treatment of cutaneous melanoma.

Declaration of competing interest

The authors declare that they have no known competing financial interests or personal relationships that could have appeared to influence the work reported in this paper.

CRediT authorship contribution statement

Jing Li: Writing – original draft, Visualization, Validation, Methodology, Investigation, Conceptualization. **Jie Wang:** Visualization, Methodology, Investigation, Data curation. **Bingqian Li:** Visualization, Investigation. **Meng Long:** Validation, Investigation, Data curation. **Xiumei Liu:** Visualization, Investigation. **Dengxuan Mao:** Visualization, Methodology. **Patrick Pan:** Visualization, Validation. **Ying Liu:** Validation, Supervision. **Zimei Wu:** Writing – review & editing, Supervision, Resources, Project administration. **Yaqi Lyu:** Writing – review & editing, Writing – original draft, Supervision, Resources, Project administration, Funding acquisition, Conceptualization. **Nianping Feng:** Writing – review & editing, Supervision, Resources, Project administration, Funding acquisition, Conceptualization.

Acknowledgments

This study was supported by Program for Shanghai High-Level Local University Innovation Team (No. SZY20220315, China), and

Shanghai Sailing Program (No. 23YF1447300, China), and Distinguished Doctoral Training Program in Key Fields for 2023 at Shanghai University of Traditional Chinese Medicine (No. GJ2023026).

Supplementary materials

Supplementary material associated with this article can be found, in the online version, at doi:10.1016/j.cclet.2025.111878.

References

[1] J. Zhang, D. Huang, P.E. Saw, E. Song, Trends Immunol. 43 (2022) 523–545.
[2] A.D. Waldman, J.M. Fritz, M.J. Lenardo, Nat. Rev. Immunol. 20 (2020) 651–668.
[3] J. Naidoo, D.B. Page, B.T. Li, et al., Ann. Oncol. 26 (2015) 2375–2391.
[4] G. Kroemer, C. Galassi, L. Zitvogel, Nat. Immunol. 23 (2022) 487–500.
[5] B. Yu, Y. Wang, T. Bing, et al., Adv. Mater. 36 (2024) e2310456.
[6] D.V. Krysko, A.D. Garg, A. Kaczmarek, et al., Nat. Rev. Cancer 12 (2012) 860–875.
[7] W. Qin, L. Qiao, Q. Wang, et al., ACS Nano 18 (2024) 1582–1598.
[8] K.N. Koch, M.L. Hartung, S. Urban, et al., J. Clin. Invest. 125 (2015) 3297–3302.
[9] R. Rouf, S.J. Uddin, D.K. Sarker, et al., Trends Food Sci. Technol. 104 (2020) 219–234.
[10] T. Dilxat, Q. Shi, X. Chen, X. Liu, Aging 16 (2024) 6521–6536.
[11] X. Zhu, R. Lu, G. Zhang, et al., Biosci. Biotechnol. Biochem. 86 (2022) 1552–1561.
[12] C. Xie, X. Zhou, W. Chen, et al., Chem. Biol. Interact. 397 (2024) 111083.
[13] J. Wu, G. Yu, X. Zhang, et al., Carbohydr. Polym. 344 (2024) 122530.
[14] C. Yunna, H. Mengru, W. Lei, C. Weidong, Eur. J. Pharmacol. 877 (2020) 173090.
[15] J. Xu, Y. Yu, Y. Zhang, et al., Nat. Nanotechnol. 19 (2024) 1569–1578.
[16] T. Moniz, S.A. Costa Lima, S. Reis, Carbohydr. Polym. 266 (2021) 118098.
[17] Z. Li, H. Lu, L. Fan, et al., Adv. Sci. 11 (2024) e2406942.
[18] Y. Hu, Y. Miao, Y. Zhang, et al., ACS Nano 18 (2024) 27557–27569.
[19] Y. Ren, L. Mei, C. Huang, et al., ACS Mater. Lett. 5 (2023) 225–234.
[20] X. Sang, T. Gao, X. Liu, et al., Adv. Sci. 9 (2022) e2201834.
[21] X. Liang, M. Mu, B. Chen, et al., Mater. Today Adv. 16 (2022) 100308.
[22] Y. Wei, X. Cai, Q. Wu, et al., Bioengineering 10 (2023) 1199.
[23] J. Lan, R. Zeng, Z. Li, et al., Adv. Mater. 36 (2024) e2408511.
[24] R. Nordstrom, K.L. Browning, E. Parra-Ortiz, et al., J. Colloid Interface Sci. 562 (2020) 322–332.
[25] C.G. Flores-Hernandez, J. Lopez-Barroso, B.A. Salazar-Cruz, et al., Polymers 16 (2024) 289.
[26] H. Chen, H. Xue, H. Zeng, et al., Biomater. Res. 27 (2023) 137.
[27] Z. Sartawi, C. Blackshields, W. Faisal, J. Control. Release 348 (2022) 186–205.
[28] H. Bian, D. Ma, X. Zhang, et al., Small 17 (2021) e2100398.
[29] Y. Wang, W. Gao, X. Shi, et al., Nature 547 (2017) 99–103.
[30] N. Zaffaroni, G.L. Beretta, Int. J. Mol. Sci. 24 (2023) 1285.
[31] C. Rogers, D.A. Erkes, A. Nardone, et al., Nat. Commun. 10 (2019) 1689.
[32] W. Li, X. Hu, S. Wang, et al., Int. J. Biol. Macromol. 145 (2020) 985–997.
[33] S. Zhang, Z. Li, X. Wang, et al., Carbohydr. Polym. 246 (2020) 116567.
[34] Y. Wang, Q. Zhao, B. Zhao, et al., Adv. Sci. 9 (2022) e2105631.
[35] P. Zheng, J. He, Y. Fu, et al., ACS Nano 18 (2024) 6863–6886.
[36] X. Dai, L. Lu, S. Deng, et al., Theranostics 10 (2020) 9332–9347.
[37] M.H. Orzalli, A. Prochera, L. Payne, et al., Immunity 54 (2021) 1447–1462.
[38] K. Chen, H. Lin, X. Peng, et al., Chin. Chem. Lett. 36 (2025) 110045.
[39] Q. Wang, X. Ju, J. Wang, et al., Cancer Lett. 438 (2018) 17–23.
[40] X. Liang, M. Mu, B. Chen, et al., Biomater. Res. 27 (2023) 120.
[41] X. Li, F. Xiong, X. Cao, et al., Chin. Chem. Lett. 37 (2026) 110970.
[42] X.T. Liu, L.H. Chung, D. Liu, et al., Oncogenesis 11 (2022) 67.
[43] X. Zhao, L.Y. Wang, J.M. Li, et al., Adv. Sci. 8 (2021) e2101498.
[44] Z. Zheng, Y. Bian, Y. Zhang, G. Ren, G. Li, Cell Cycle 19 (2020) 1089–1104.
[45] F. Yao, Z. Jin, Z. Zheng, et al., Cell Death Discov. 8 (2022) 112.
[46] A.C. Huang, R. Zappasodi, Nat. Immunol. 23 (2022) 660–670.
[47] S. Kalaora, A. Nagler, J.A. Wargo, Y. Samuels, Nat. Rev. Cancer 22 (2022) 195–207.
[48] C. Scirgolea, R. Sottile, M. De Luca, et al., Nat. Immunol. 25 (2024) 1845–1857.